Strong Plates Enhance Mantle Mixing in Early Earth

Roberto Agrusta[1,*], Jeroen van Hunen[1] and Saskia Goes[2]

[1]Department of Earth Sciences, Durham University, Durham, UK

[2]Department of Earth Science and Engineering, Imperial College London, London, UK

[*]presently at: Laboratoire de Géologie de Lyon, Université de Lyon, École Normale Supérieure de Lyon, Lyon, France

Corresponding author: Roberto Agrusta (roberto.agrusta@ens-lyon.fr)

Abstract

In the present-day Earth, some subducting plates (slabs) are flattening above the upper-lower mantle boundary at ~670 km depth while others go through, indicating a mode between layered and whole-mantle convection. Previous models predicted that in a few hundred degree hotter early Earth, convection was likely more layered due to dominant slab stagnation. In self-consistent numerical models where slabs have a plate-like rheology, strong slabs and mobile plate boundaries favour stagnation for old and penetration for young slabs, as observed today. We now show that such models predict slabs would have penetrated into the lower mantle more easily in a hotter Earth, when a weaker asthenosphere and decreased plate density and strength resulted in subduction almost without trench retreat. So heat and material transport in the Earth's mantle was more (rather than less) efficient in the past, which better matches the thermal evolution of the Earth.

Introduction

Seismic imaging of Earth's mantle has shown that when subducting plates reach the upper-lower mantle boundary at ~670 km depth, they can either penetrate straight into the lower mantle or flatten in the mantle transition zone above this boundary[1,2] (Figure 1a). How easily slabs penetrate into the lower mantle exerts a key control on the efficiency of mass and heat flux across the mantle between the surface and the boundary with the outer core, to which active upwellings probably contribute only 10-20% to the total heat transport[3,4]. The mix of temporarily stagnant and penetrating slabs in the mantle transition zone indicates that the present-day mantle is in a transitional mode between layered and whole convection[5,6]. However, convection style might have changed during the Earth's history as mantle temperatures decreased by 200-300°C from the Archean eon to the present[7,8], and previous convection studies predict that this mantle cooling would switch convection style from a dominantly layered system in the past to a system intermediate between whole and layered at the present day[6,9,10] (Figure 1b).

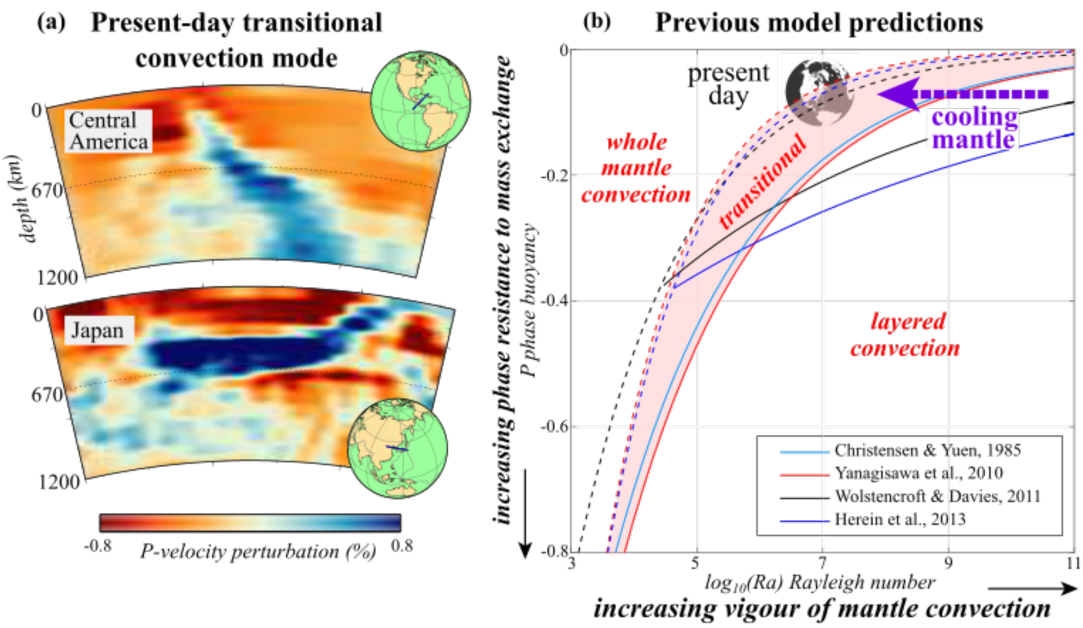

Figure 1 – **Present and previously predicted mantle convection styles.** (a) Examples from seismic tomography of a slab readily penetrating the transition zone (below Central America) and a slab that has ponded (below Japan) [11]. (b) Regime diagram showing how previous studies [5,6,9,12] predict that the style of mantle convection varies with buoyancy number P (the ratio of the phase buoyancy of the endothermic phase transition hampering slab sinking over the thermal buoyancy which drives slab sinking) and Rayleigh number (the ratio of convection-driving over convection-resisting forces, which increases proportionally to mantle temperature). All studies agreed that the critical phase buoyancy required to layer convection decreases (becomes less negative) with increasing Rayleigh number. The Earth logo represents the estimated present-day conditions [from ref. [6]], and the arrow the likely change from layered convection in an early Earth to a transitional mode today.

The upper-lower mantle boundary coincides with the endothermic phase transition in the main mantle mineral olivine, from its ringwoodite (rg) phase to its denser post-spinel assemblage (perovskite and magnesiowustite, pv+mw), and it likely also localises at least part of the factor 10-100 viscosity increase from upper to lower mantle[13,14]. This phase transition gets depressed to larger depths inside the cold slab from its equilibrium depth (~670 km) and might hamper the flow across it. This deflection depends on the phase transition Clapeyron or pressure-temperature slope and if the Clapeyron slope is strong (negative) enough, it can break mantle convection into two layers[6,9,12,15]. Whether convection is layered or not depends on whether the positive phase buoyancy of the endothermic transition exceeds the negative thermal buoyancy of the slabs, and it has been demonstrated that the necessary critical buoyancy number P (the ratio of the phase and thermal buoyancy, eq. M4) to induce layered convection by the endothermic phase transition decreases with increasing convective vigour, i.e., increasing mantle temperature (Rayleigh number, eq. M3) [5,6,9] (Figure 1b). This stronger propensity for layering at higher Rayleigh number has been attributed to the lower viscosity and smaller scale of down- and upwellings in a hotter mantle[9,16], which makes the transmission of the thermal buoyancy forces, necessary to overcome the effect of an endothermic phase transition, less efficient. This was found to hold in both models with an isoviscous mantle[6,9,12] and in models that test the effect of temperature-dependent and/or stress-dependent viscosity, which leads lithosphere and slabs to behave more plate-like[5,16]. So it is generally assumed that the previously hotter mantle convected in a more layered style.

On Earth, its observed that older (denser and stronger) plates have a higher tendency to produce trench retreat and flat slabs above the upper-lower mantle boundary around ~670 km depth than young plates[17,18]. This behaviour is reproduced in recent dynamical models where plate boundaries move in response to the slab dynamics. In these models[2,19–22], stronger and denser (old) slabs interacting with both an endothermic phase change and viscosity increase induce trench retreat and stagnate (at least for 10s to 100s of m.y.), while weaker and lighter (young) slabs accumulate at relatively stationary trenches, which aids penetration. While other factors, like for example the persistence of metastable phases in the slab's coldest core and associated slab weakening[17,23–25], may additionally hamper the sinking of older slabs through the transition zone, variable plate age at the trench can explain the primary observations of today's mixed slab-transition-zone dynamics and its relation to trench motion[2,21]. In this study, we use these calibrated models to re-examine how such more plate-like and mobile slabs behave under hotter mantle conditions. The new results show that, contrary to previous work, higher mantle temperatures favour less layered convection with decreased slab stagnation in the transition zone, which has important consequences for Earth's evolution.

Results

In this study, it has been performed a set of 35 numerical simulations with the dynamically self-consistent thermo-mechanical 2D subduction models of Agrusta et al.[19] (see methods, Supplementary Table S1) to investigate how old (100 Myr) and young (50 Myr) plates interact with a phase and viscosity boundary at different mantle temperatures. Mantle potential temperatures (i.e., temperatures at the top of the convective mantle geotherm, the mantle adiabat) are varied from 50 °C cooler to 200 °C hotter than the present-day. This results in a mantle viscosity jump at the upper-lower mantle boundary between a factor of 10 (at present-day conditions) to a factor of 40 (in the hotter mantle). The models include the two main olivine phase transitions, the exothermic olivine to wadsleyite, ol-wd, transition at ~410 km depth, and the rg-pv+mw at ~670 km. To test the effect of phase buoyancy P, the Clapeyron slopes have been varied over a plausible range, from 3 $\mathrm{MPa{\cdot}K^{-1}}$ to 5 $\mathrm{MPa{\cdot}K^{-1}}$ (ol-wd)[26,27] and from -1 $\mathrm{MPa{\cdot}K^{-1}}$ (P =-0.036) to -3 $\mathrm{MPa{\cdot}K^{-1}}$ (P =-0.109) (rw-pv + mw)[28,29]. The models presented use a Newtonian rheology and assume a composition of 100 wt% of olivine, but additional models, with a composite non-Newtonian creep and only 60 wt% of olivine, that display the same styles of behaviour are in the Supplement. In three additional simulations, the effect of slab strength at transition zone depths has been investigated, by reducing slab viscosity below 400 km depth.

Present-day subduction dynamics

The present-day models produce the mixed stagnation-penetration style where older, colder plates have a stronger tendency to stagnate and younger plates to penetrate[17,18]. Figure 2a,b illustrates how a young, hot, and weak subducting plate drives only modest trench retreat and therefore penetrates directly into the lower mantle, while an old, cold, and strong plate sinks with significant trench retreat, and flattens in the transition zone[2,19].

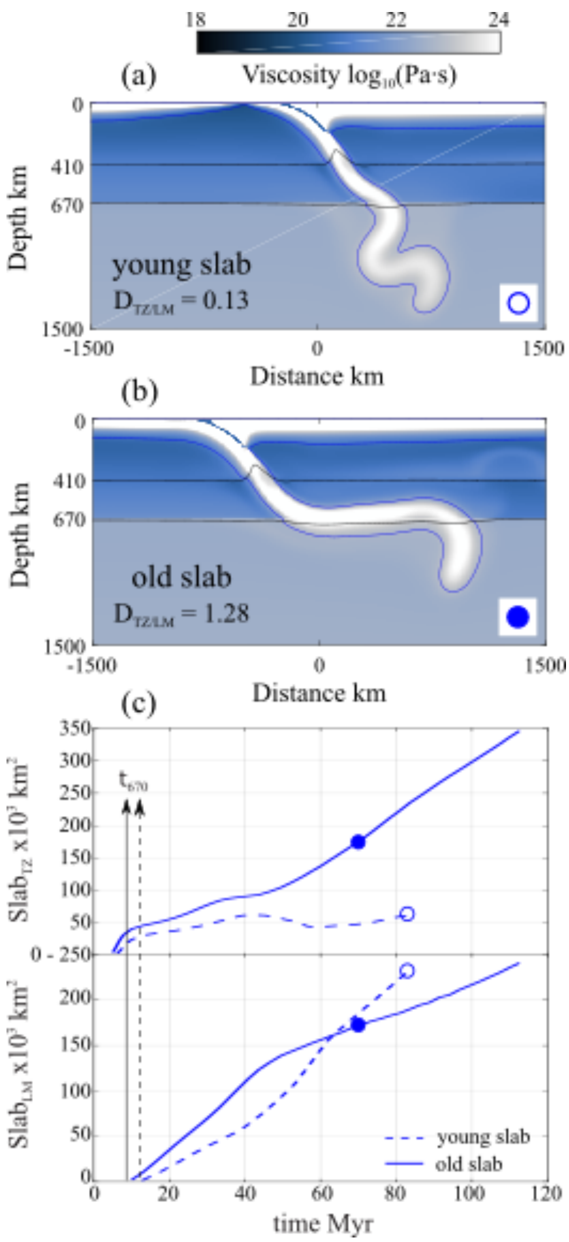

Figure 2 - **Slab dynamics for present-day mantle temperature**. Cases shown are a young penetrating slab (Simulation 11, open blue circle) (a), and old flattened slab (Simulation 12, solid blue circle, see Table S1) (b). The initial trench is located at x = 0 km. The blue line is the contour delimiting the slab at constant potential temperature of 1300°C. For both cases the value of the slab accumulation rate $D_{TZ/LM}$ is indicated (c) Evolution of the volume of slab material in transition zone ($Slab_{TZ}$) and lower mantle ($Slab_{LM}$). The dots mark the time of the snapshots in (a-b). While significant volumes of the old slab (solid lines) accumulate in the transition zone, most of the young slab material (dashed lines) goes straight through. The arrows mark the times at which the slabs reach the 670 km depth (t_{670}).

A useful measure for slab penetration into the lower mantle is to compare the accumulated volume of slab material in the transition zone (‘$Slab_{TZ}$’) and the lower mantle (‘$Slab_{LM}$’) through time (Figure 2c). In the stagnant case, $Slab_{TZ}$ increases more quickly than $Slab_{LM}$, because a significant part of the slab accumulates in the transition zone. In contrast, for the penetrating young slab, the amount of slab material that collects in the transition zone is low and almost constant during the simulation time. This behaviour can be summarised by a slab accumulation rate (D) in each mantle layer (D_{TZ} and D_{LM}), calculated as:

$$D_{TZ/LM} = \frac{Slab_{TZ/LM}\left(\tau_{end}\right) - Slab_{TZ/LM}\left(\tau_{670}\right)}{time\left(\tau_{end}\right) - time\left(\tau_{670}\right)}, \quad (1)$$

where τ_{670} and τ_{end} correspond to the model time at which the slab reaches the base of the upper mantle (670 km) and the end time of the simulation, respectively. The ratio D_{TZ}/D_{LM} is used to classify slab penetration or stagnation, with values >1 for significantly stagnating slabs and <1 for mostly penetrating slabs.

Dynamics in a hotter mantle

The effects of a hotter mantle are shown in Figure 3 through snapshots of old-slab simulations at two different model times for the most negative Clapeyron slope, i.e., the cases most likely to stagnate (for times of 80 m.y. or longer). At present-day temperatures ($\Delta T_{\mathrm{pot}} = 0$ °C, Figure 3a), the slab flattens at the base of the upper mantle similarly to the case shown in Figure 2b, as can be seen in the evolution of $Slab_{TZ}$ and $Slab_{LM}$ (Figure 3e,f, blue lines), with lower-mantle slab penetration even more reduced due to the stronger Clapeyron slope. At higher mantle temperatures (Figure 3b,c,d), the slab folds and piles up in the transition zone. When a sufficiently large volume of slab has accumulated in the transition zone, its negative buoyancy is able to overcome the phase resistance, and the slab starts sinking into the lower mantle. Figure 3e,f further illustrate how the slab initially accumulates in the transition zone ($Slab_{TZ}$ increasing), followed by a relatively stable phase where slab material slowly increases in the lower mantle ($Slab_{LM}$ increasing), and a final stage in which $Slab_{TZ}$ decreases, and the slab sinks more rapidly into the lower mantle. The time towards this accelerated slab lower-mantle sinking decreases with increasing Rayleigh number.

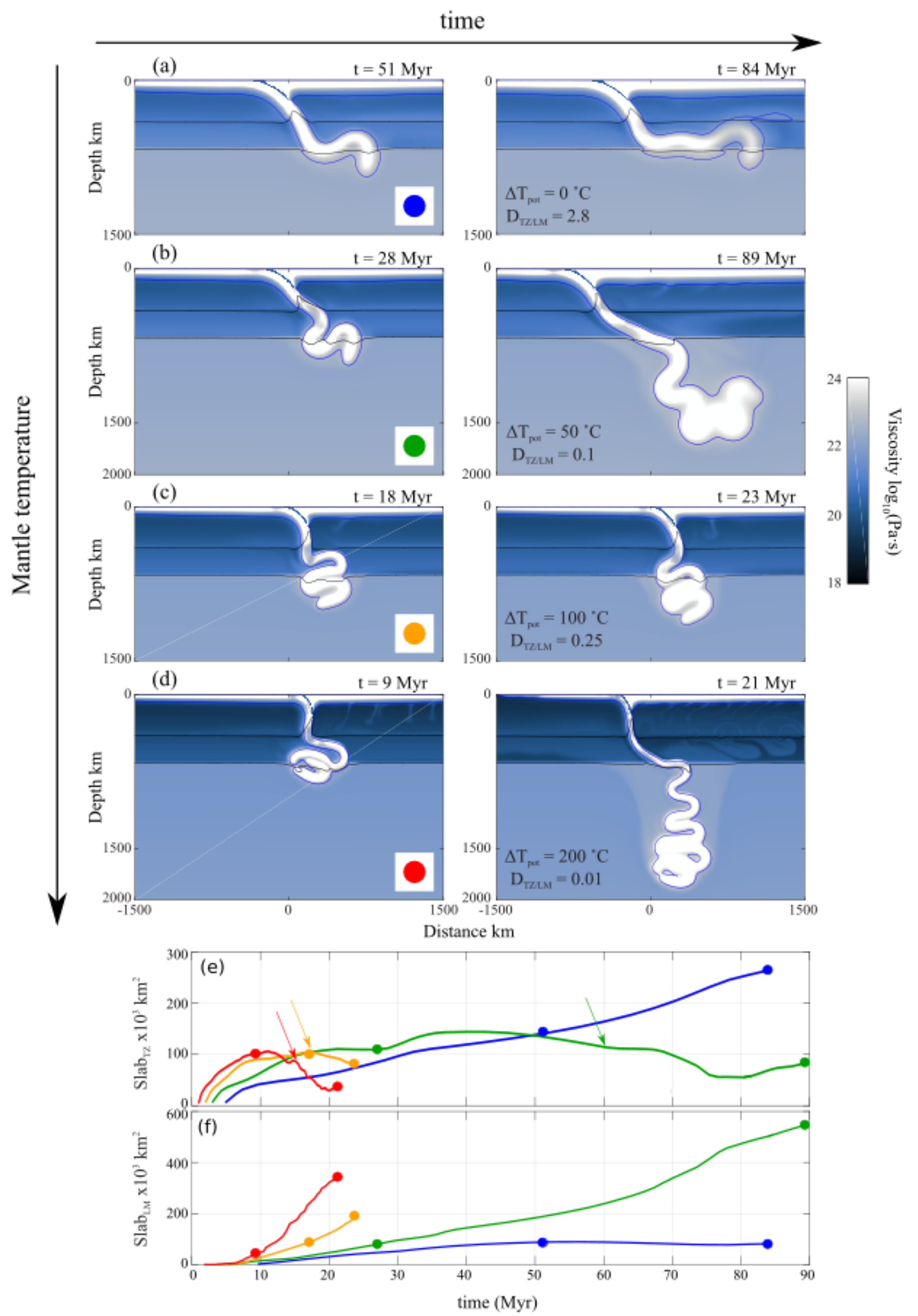

Figure 3 – **Penetrating slabs in a hotter mantle**. (a-d) Old (initial age 100 Myr) slab evolution for different mantle temperatures (illustrated by two snap shots each) at strongly negative postspinel Clapeyron slope (-3 MPa/K) (Simulations 16, 20, 26 and 32, Table S1): (a) present-day temperature, ΔT_{pot} = 0 °C (blue), (b) ΔT_{pot} = +50 °C (green), (c) ΔT_{pot} = +100 °C (orange), (d) ΔT_{pot} = +200 °C (red). This colour coding is subsequently used in (e,f), and Figure 4. For each case the value of $D_{TZ/LM}$ is indicated. The evolution of slab material in the transition zone $Slab_{TZ}$ (e) and lower mantle $Slab_{LM}$

(f). The arrows in (e) indicate the approximate timing of accelerated lower-mantle slab sinking events in the hotter mantle models. The dots mark the timing of the snapshots in (a-d)

The slab accumulation rates D_{TZ} and D_{LM} and their ratios for all cases, including different slab ages and Clapeyron slopes are compiled in Figure S1. All slabs in the hotter mantle models (ΔT_{pot} = 100 °C and 200 °C), irrespective of the initial slab ages, have high D_{LM} and low D_{TZ} and D_{TZ}/D_{LM} <1, indicating easy penetration into the lower mantle. In contrast, slabs in a colder mantle (ΔT_{pot} = 0 °C and -50 °C) have lower D_{LM} and higher D_{TZ} and some stagnate in the transition zone while others penetrate easily. For weaker phase-transition resistance (less negative Clapeyron slope values), all slabs tend to penetrate directly into the lower mantle, whereas for more negative Clapeyron slope values, easy stagnation occurs for plates with old initial ages.

Figure 4 summarises these results in a regime diagram of slab-transition zone interaction style as a function of Rayleigh and phase buoyancy numbers, similar to what was done in previous studies[5,6,12] (Figure 1b). Layered convection, where slab stagnation occurs for both young and old plates, is only achieved at low Rayleigh number (i.e., cooler Earth than today) and low phase buoyancy number (most negative Clapeyron slope). At intermediate P and Ra, both modes are found, with easy penetrating young and long temporal stagnant old slabs. At higher Ra (hotter Earth), no slab stagnation is observed. Note that these boundaries can shift within the uncertainties and trade-offs between model parameters. At a higher viscosity jump at the base of the transition zone, the field of stagnant and mixed modes expands to lower phase buoyancy and higher Ra. A reduction of the asthenospheric mantle viscosity, leading to less trench mobility[30,31], would induce an opposite shift. The main features of the regime diagram as a function of temperature are however robust.

In a cooler Earth, older stronger slabs are able to drive trench retreat, which lays out the slabs in the transition zone, hampering their entrance into the lower mantle. At higher temperatures, trench retreat is discouraged by lower slab strength, which facilitates plate bending, and decreases asthenospheric viscosities, which inhibits trench retreat [32,33]. These factors, together with a lower resistance from a hotter, and therefore less viscous lower mantle, allow slabs in a hotter mantle to enter the lower mantle more easily than at modern mantle temperatures. Given that today's mantle is in a mixed mode, these models imply that mantle cooling increases the occurrence of slab stagnation, and, in contrast to what was found in earlier studies, in a hotter Earth, slab penetration would have been dominant.

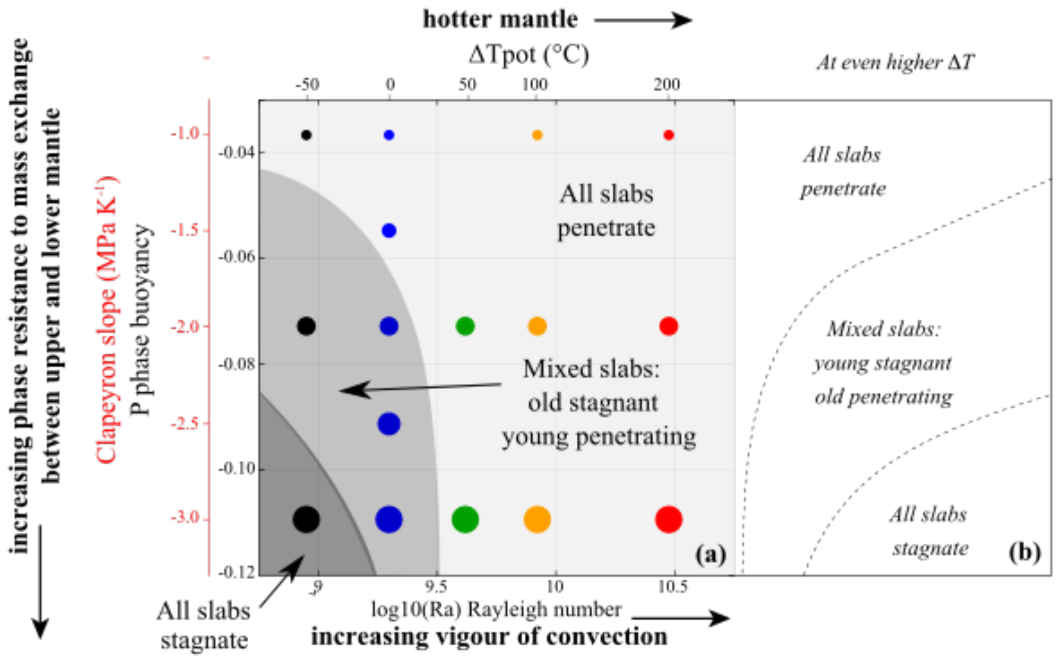

Figure 4 – **Mantle mixing modes at different mantle temperatures**. Regime diagram obtained from all our simulations (coloured dots) as a function of the phase buoyancy number *P* (and corresponding Clapeyron slope) for the endothermic phase transition and Rayleigh number (and corresponding mantle temperature). Note that the Ra of our regional models are not directly comparable to those of the global-scale models in Figure 1b, but present-day Earth conditions are likely somewhere around the middle blue dot. Dark grey field covers the domain of pure slab stagnation, middle grey the domain for young slab penetration and old slab stagnation, light grey field the domain of pure slab penetration. On the right side, the regime diagram is schematically extended as expected at even higher temperature from the results of our weak slabs models together with results from previous models where plates were weak and trenches less mobile.

Slab strength

Slab weakening in the transition zone, which can be due to grain size reduction during phase transformation, has been previously proposed to lead to slab stagnation[17]. The slabs presented here are stronger than in previous models, allowing them to penetrate the endothermic phase transition even when the mantle temperature is increased by 200 degrees. To investigate whether slab strength accounts for this different model behaviour, one of the models has been re-run with a weaker slab in and below the transition zone, by reducing the maximum viscosity below 400 km depth to 10^{23} Pa·s, 5×10^{22} Pa·s, and 10^{22} Pa·s (Figure 5). These weaker slabs deform considerably when they reach the bottom of the upper mantle, spreading out in the transition zone. The weakest slabs, with viscosities of only a few times the background mantle viscosity, fail to enter the lower mantle (Figure 5c). Most likely, previous studies that concluded that stagnation increases with Ra, investigated a regime where already weak slabs become even weaker under hotter mantle conditions, which leads to increasing stagnation. This behaviour might be expected for the presented models as well if mantle temperature is raised further (i.e. for much higher Ra) (Figure 4). In an intermediate regime between hot penetrating slabs and even hotter stagnant ones, the weakest (youngest) slabs would stall while the colder stronger ones would still be able to penetrate, opposite to what happens in the mixed mode of present-day models[19] and what is observed on Earth[2,17,18].

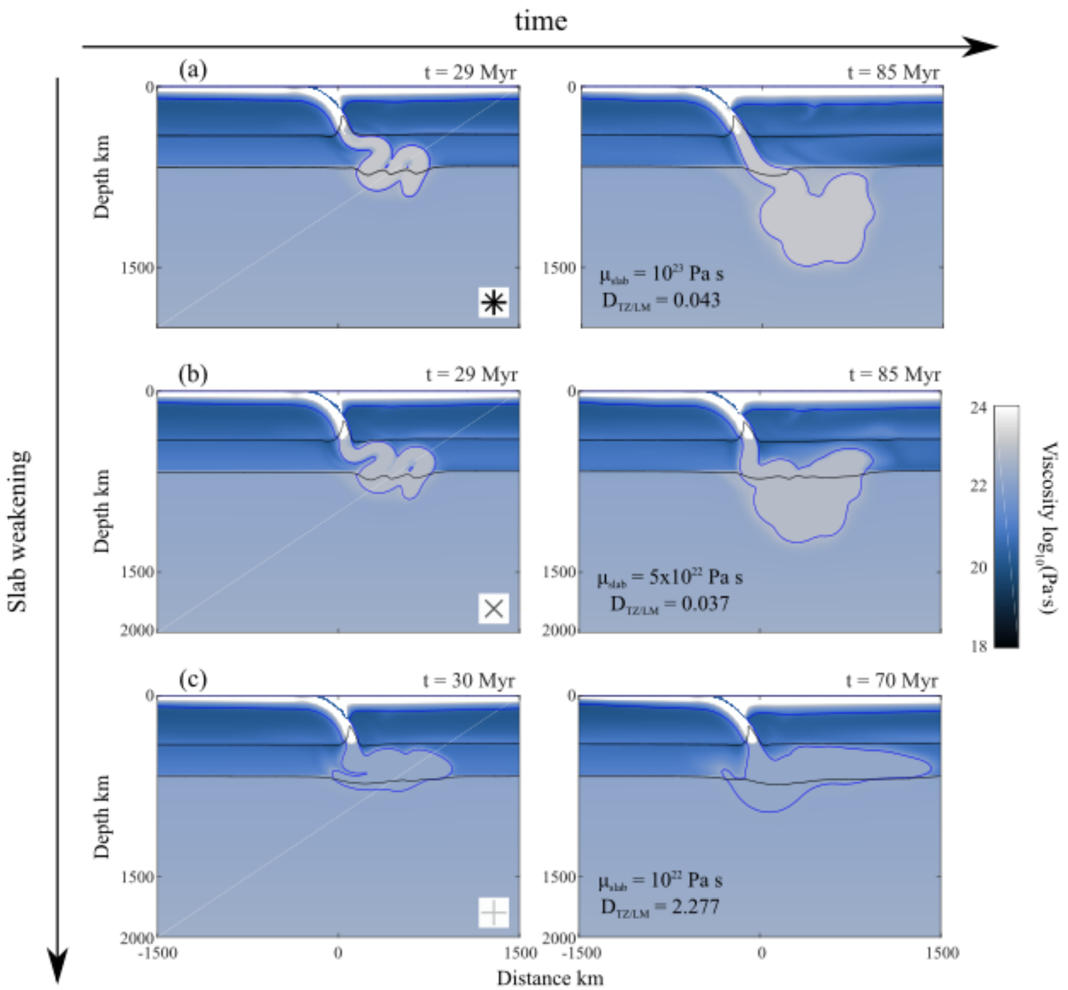

Figure 5 - **Weaker slab interaction with the upper-lower mantle boundary**. Slab evolution of simulations 20a,b,c in which the maximum viscosity cut off below 400 km depth is reduced to: (a) 10^{23} Pa·s, (b) 5×10^{22} Pa·s, and (c) 10^{22} Pa·s. For the three cases the value of $D_{TZ/LM}$ is indicated, highlighting how very weak transition-zone slabs tend to stagnate.

Discussion and Conclusions

Potential other factors affecting Early Earth subduction

Several factors not accounted for in this work may affect slab dynamics in a hotter mantle, most notably the effects of a higher melting degree on plate buoyancy and strength[34,35]. High mantle temperatures in the past could have produced thicker oceanic crust at mid ocean ridges[36] and leave behind a water-depleted stiffer lithosphere. Based on previous studies, possible implications are discussed:

(i) *Crustal buoyancy.* A thicker and more buoyant crust would probably resist subduction, similar to modern aseismic ridges, but may not prevent it[37], and could have made subduction episodic[34]. Moreover, a lower-density, but still subductable crust leads to a subduction style that would look like continental subduction, in which trench retreat is usually absent[38], and hence encourages penetration[19,20]. Some studies suggest that the early Earth oceanic crust compositions would be denser than ambient mantle[39], which instead would have further have facilitated subduction and probably lower-mantle penetration.

(ii) *Melt-depletion.* A lithosphere that is substantially dehydrated upon melt extraction may be between a factor 2-3 to 100 stronger than hydrated plates [40–42]. The effect of strengthening by dehydration may be partially or totally negated by melt weakening[43], or rehydration in bending faults at the trench [44]. Note that when slabs become significantly stronger than the present-day effective slab bending strength, subduction will stop completely because plate bending can no longer be achieved with the available slab potential energy [45], so during the time over which subduction has been active, plates were probably never more than a few times stronger than those at the present-day. However, even if slab strength decreased less rapidly with increasing mantle temperature than in the presented models because of a trade-off with strengthening by dehydration, a weaker lower mantle would still enhance penetration [19,46], and the transitional mode may prevail to somewhat higher temperatures than the presented models predict before all slabs start to penetrate.

(iii) Metastable phases inside the coldest slabs have been proposed to contribute to the stagnation of older plates in the transition zone[17,18,23,25] However, at higher temperatures both the effects of metastability and concurrent slab weakening due to grain size reduction will be suppressed, thus also facilitating slab penetration in a hotter Earth.

Implications and consequences

Presently subducting slabs exhibit mixed behaviour in the transition zone, where older plates have a tendency to stagnate, while younger ones penetrate easily into the lower mantle. Models in which slabs have plate-like rheology and trenches are mobile reproduce this behaviour, and show that slabs would have been sinking more easily into the lower mantle in a hotter, earlier Earth. This would have allowed the early Earth to cool and mix mantle heterogeneities more efficiently than occurs at the present-day. Some studies have argued that dense piles in the deep mantle, suggested to be the cause of the seismic large-low shear velocity provinces, have been in stable locations for half a billion years or more[47,48]. This is difficult in a system of efficient whole mantle convection[49–52], like the presented models predict for much of Earth evolution.

The presented study does ignore the active upwelling part of the global convection. As mentioned in the introduction, upwellings probably contribute only ~10-20 % of present-day mantle heatflux[3,4]. Furthermore, upwellings are expected to readily cross the phase transition at hotter mantle conditions because for transition-zone temperatures higher than 2000°C, the transition in a pyrolite or harzburgite composition to postspinel phases at the base of the upper mantle becomes exothermic (positive Clapeyron slope)[53] which facilitates material flow through the phase transition.

The presented results contrast with previous modelling studies[5,6,9,12,16] that predicted that, in a hotter mantle, the phase and viscosity changes at the base of the transition would have increasingly hampered slab sinking into the lower mantle and thus would have led to layered convection in upper and lower mantle. The behaviour that the presented models predict reconciles dynamics with cooling history calculations. Layered convection would not have cooled the early Earth efficiently enough to explain present day heat flow and mantle temperature[54]. Davies[55] proposed full mantle layering in an early Earth that would periodically collapse into catastrophic mantle overturns, a mechanism that would have allowed cooling in spite of layering. Instead, with the new results slab sinking into the lower mantle may have happened efficiently by regional lower-mantle sinking events.

So early-Earth slabs probably favoured lower-mantle penetration and promoted whole-mantle convection. However, before plate tectonics started, perhaps around 3 Ga[56–58], downwellings were probably more random, in the form of small-scale features[59], and this would have made mass exchange between upper and lower mantle less efficient. Consequently, the Earth may have undergone more mixing throughout its 'middle ages', and less so in its 'youth' and 'old age'.

Method

Governing physics

The slab-transition zone interaction is studied with 2D self-consistent subduction simulations using the finite-element code CITCOM[60–62]. The code solves the system of conservation of mass, momentum, and energy equations, for an incompressible fluid, at infinite Prandtl number, under the extended Boussinesq approximation[9], without internal heating.

The mantle phase transitions are included using a harmonic phase function[23]. The relative fraction of the heavier phase is described by the phase function Γ, varying from 0 and 1 as a function of pressure and temperature, as:

$$\Gamma_i = 0.5\left[1+\sin\left(\frac{z-z_i-\gamma_i\left(T_{pot}-T_i\right)}{d_i}\right)\right], \qquad \text{(M1)}$$

where d_i is the width of the transformation in depth, γ_i is the Clapeyron slope, and z_i and T_i are the depth and temperature of the i*th* mantle phase transition at equilibrium conditions, respectively. z and T_{pot} are depth and potential temperature.

The rheological model is assumed to be a combination of linear diffusion creep (μ_{diff}) and a pseudo-brittle yield stress rheology (μ_y). The effective viscosity μ_{eff} is calculated from the viscosities of the individual mechanisms as:

$$\mu_{eff} = \min\left(\mu_{diff}, \mu_y\right), \qquad \text{(M2.a)}$$

with

$$\mu_{diff} = \Delta\mu_{lower/upper} A_{diff} \exp\left(\frac{E_{diff}+PV_{diff}}{RT}\right) \qquad \text{(M2.b)}$$

and

$$\mu_y = \frac{\min\left(\sigma_0 + f_c P, \sigma_{max}\right)}{\dot{\varepsilon}_{II}}. \qquad \text{(M2.c)}$$

The factor $\Delta\mu_{lower/upper}$ defines the viscosity jump at 670 km depth, and reduces to 1 in the upper mantle. A_{diff}, V_{diff} and V_{diff} are the pre-exponential factor, activation energy and activation volume, respectively. R is the gas constant, T the absolute temperature, and P the lithostatic pressure. σ_0 and $\sigma_{\max}$ are surface and maximum yield strength, f_c is the friction coefficient, and $\dot{\varepsilon}_{II}$ the second invariant of the strain rate. A viscosity cutoff is imposed for numerical stability, and is 10^{24} Pa s, unless mentioned otherwise. The values of all model parameters are listed in Table M1. For more model setup details, the reader is referred to Agrusta et al.[19].

Table M1 - List of parameters

Symbol	Meaning	Unit	Value
	Global parameters		
H	Box height	km	3000
ΔT	Potential temperature drop	°C	1300
T_{pot}	Potential temperature	°C	$1300 + \Delta T_{pot}$
ΔT_{pot}	Temperaure increase	°C	(-50 to 200)
ρ_0	Surface reference density	$kg \cdot m^{-3}$	3300
g	Gravity	$m \cdot s^{-2}$	9.8
α_0	Surface thermal expancivity	K^{-1}	3×10^{-5}
κ	Thermal diffusivity	$m^{-2} \cdot s^{-1}$	10^{-6}
μ_0	Reference viscosity	Pa·s	$\mu_{eff}(z=0,T=T_{pot})$
C_P	Heat capacity	$J \cdot kg^{-1} \cdot K^{-1}$	1250
R	Gas constant	$J \cdot mol^{-1} \cdot K^{-1}$	8.314
	Rheological model parameters		
	Diffusion creep		
A_{diff}	Pre-exponential upper mantle	Pa·s	1.87×10^{9}
	Pre-exponential lower mantle		2.29×10^{14}
E_{diff}	Activation energy upper mantle	$J \cdot mol^{-1}$	3×10^{5}
	Activation energy lower mantle		2×10^{5}
V_{diff}	Activation volume upper mantle	$m^3 \cdot mol^{-1}$	5×10^{-6}
	Activation volume lower mantle		1.5×10^{-6}
$\Delta\mu_{lower/upper}$	Viscosity jump	-	10
	Byerlee's plastic deformation		
f_c	Friction coefficient	-	0.2
σ_{max}	Maximum yield strength	MPa	300
σ_{max}	Surface yield strength	MPa	20
	Mantle phase transition parameters		
$\gamma_{ol\text{-}wd}$	Clapeyron slope ol-wd transition	MPa/K	(2.5 to 5)
$\gamma_{rw\text{-}pv+mw}$	Clapeyron slope rg-pv+mw transition	MPa/K	(-0.5 to -3)
$z_{ol\text{-}wd}$	Central ol-wd transition depth	km	410
$z_{rw\text{-}pv+mw}$	Central rw-pv+mw transition depth	km	670
$d_{ol\text{-}wd}$	ol-wd transition width	km	20
$d_{rw\text{-}pv+mw}$	rg-pr+mw transition width	km	20
$T_{ol\text{-}wd}$	ol-wd transition potential temperature	K	T_{pot}
$T_{rw\text{-}pv+mw}$	rg-pr+mw transition potential temperature	K	T_{pot}
$\Delta\rho_{ol\text{-}wd}$	ol-wd transition density contrast	$kg\ m^{-3}$	250
$\Delta\rho_{rw\text{-}pv+mw}$	rg-pr+mw transition density contrast	$kg\ m^{-3}$	350

Model set-up

The model domain is 9000 km wide and 3000 km high, and the box is discretized into 2880×472 elements, with element sizes ranging from 2.5 km to 7.5 km. The grid is refined vertically between 0 and 270 km depth, and horizontally between x = -5750 km and x = 900 km. The mechanical boundary conditions are free-slip along all boundaries, so only internal buoyancy forces drive the dynamics. The top and bottom thermal boundary conditions are constant temperature, 273 K at the surface and a potential T_{pot} at the bottom. The thermal boundary conditions are different at the left and right boundaries: a zero heat flux is imposed on the left boundary, whereas on the right boundary a mid-ocean ridge (MOR) temperature profile is used to keep the MOR at the model corner (Figure M1a).

The initial conditions are chosen to represent an overriding and a subducting plate, both with a half-space-cooling thermal structure [63]. The overriding plate extends from a MOR at the upper-right corner to the trench (at x = 0 km) with a plate age of 100 Myr. The initial subducting plate has slab with a radius of curvature of 500 km, and extends from the trench into the mantle down to a depth of 200 km, which allows self-sustained subduction from the start. The length of the subducting plate, and hence the location of the MOR x_{MOR}, are calculated using the initial plate velocity and age such that $x_{MOR} = -V_{SP} \cdot Age_{SP}$, where V_{SP} is the initial plate velocity and Age_{SP} is the initial subducting plate age at the trench. For each initial subducting plate age and mantle temperature, V_{SP} is determined by solving the instantaneous flow field for t = 0. Once V_{SP} is determined, it is used to calculate x_{MOR} for a self-consistent plate age distribution. V_{SP} ranges from ~3 cm·yr^{-1} (lowest T_{pot}) to ~25 cm·yr^{-1} (highest T_{pot}), and the initial subducting plate age does not significantly influence the initial V_{SP}. On top of the entire subducting plate, an 8 km thick low-viscosity layer ($\mu_{weak\text{-}layer} = 10^{20}$ Pa s) is present which extends down to 200 km depth to facilitate the decoupling of the converging plates.

Parameters to simulate Early Earth conditions

Mantle composition, and therefore mantle rheological and phase transition parameters are assumed to remain the same from the early Earth to the present-day. The mantle potential temperature is varied from its present-day reference T_{pot} = 1300 °C by a ΔT_{pot} between -50 °C (further mantle cooling) and +200 °C (hotter Earth)

(Figure M1b). Only the olivine solid-solid phase transitions are considered and the density contrasts ($\Delta\rho$) used for the olivine-wadsleyite (ol-wd, near 410 km depth) and ringwoodite-perovskite+magnesiowüstite (rg-pv+mw, near 670 km) transformations are 250 kg m^{-3} and 350 kg m^{-3}[ref 64], respectively.

Convective vigour is characterised by the thermal Rayleigh number

$$Ra = \frac{g\alpha_0\rho_0\left(\Delta T + \Delta T_{pot}\right)H^3}{\kappa\mu_0}, \quad \text{(M3)}$$

where g is the gravitational acceleration, α_0, ρ_0, μ_0 the reference thermal expansivity, density and viscosity, respectively, κ the thermal diffusivity, $\Delta T+\Delta T_{pot}$ the potential temperature contrast across the box, and H box depth (Table M1). Resistance to sinking through the 670-km phase transition is expressed in terms of the phase buoyancy number, $P = \overline{\gamma}_{rw-pv+mw}\frac{Rb_{rw-pr+mw}}{Ra}$, (M4)

with phase Rayleigh number

$$Rb_{rw-pr+mw} = \frac{g\Delta\rho_{rw-pr+mw}H^3}{\kappa\mu_0}. \quad \text{(M5)}$$

And the ol-wd phase transition is implemented similarly.

The rheological parameters (Eq. M2) have been chosen to obtain suggested present-day mantle viscosity values, such that the average upper and lower mantle viscosities are ~2×10^{20} and ~3×10^{22} Pa s, respectively[42,65–69]. At ΔT_{pot} = +200 °C, the viscosity profile reaches average values of ~1.15×10^{19} Pa s and ~4.6×10^{21} Pa s respectively for upper and lower mantle (Figure M1c).

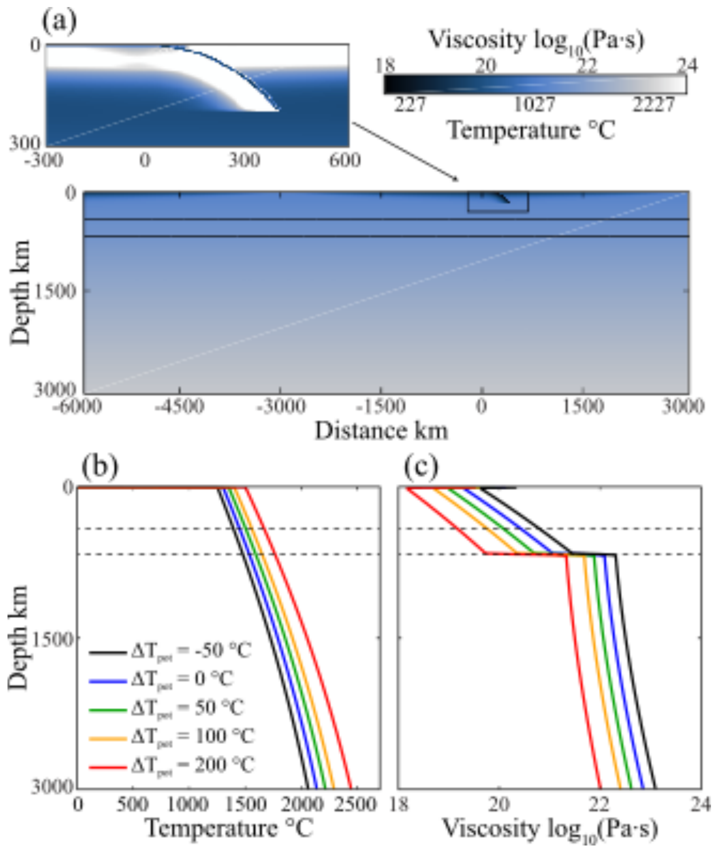

Figure M1 - **Model set-up** (a) Initial condition for a subducting plate 100 Myr old at the reference mantle temperature (ΔT_{pot} = 0 °C). Colours indicate temperature, and the horizontal black lines mark the olivine phase transitions. The zoomed area shows corresponding viscosity where the weak layer on top of the plate is visible (dark blue). Background mantle temperature (b) and viscosity (c) profiles (at the MOR) for the five investigated mantle potential temperatures. The colour scale is used to identify different model cases in the main text, and ranges from black (ΔT_{pot} = -50 °C) for the colder mantle temperature case to red (ΔT_{pot} = +200 °C) for hottest mantle case.

Acknowledgments

We would like to thank the editor Mellissa Plail and the reviewers Magali Billen and Fabio Crameri for their constructive and useful comments. The perceptually-uniform colour map oslo is used in this study to prevent visual distortion of the data. The authors acknowledge funding from the European Research Council (ERC StG 279828) and NERC (grant NE/J008028/1) and the work used the ARCHER UK National Supercomputing Service (http://www.archer.ac.uk) and appreciate the comments of D. Selby, E. Lewellin, and J. Baldini on an earlier version of the manuscript. Data for this paper can be made available upon request from the authors.

Contributions

All authors developed the concepts of the study and contributed to the writing of the manuscript. R.A. developed and analysed the models.

References

1. Fukao, Y. & Obayashi, M. Subducted slabs stagnant above, penetrating through, and trapped below the 660 km discontinuity. *J. Geophys. Res. Solid Earth* **118,** 5920–5938 (2013).
2. Goes, S., Agrusta, R., van Hunen, J. & Garel, F. Subduction-transition zone interaction: A review. *Geosphere* (2017). doi:10.1130/GES01476.1
3. Nolet, G., Karato, S. I. & Montelli, R. Plume fluxes from seismic tomography. *Earth Planet. Sci. Lett.* **248,** 685–699 (2006).
4. Davies, G. F. Penetration of plates and plumes through the mantle transition zone. *Earth Planet. Sci. Lett.* **133,** 507–516 (1995).
5. Yanagisawa, T., Yamagishi, Y., Hamano, Y. & Stegman, D. R. Mechanism for generating stagnant slabs in 3-D spherical mantle convection models at Earth-like conditions. *Phys. Earth Planet. Inter.* **183,** 341–352 (2010).
6. Wolstencroft, M. & Davies, J. H. Influence of the Ringwoodite-Perovskite transition on mantle convection in spherical geometry as a function of Clapeyron slope and Rayleigh number. *Solid Earth* **2,** 315–326 (2011).
7. Herzberg, C., Condie, K. & Korenaga, J. *Thermal history of the Earth and its petrological expression*. *Earth and Planetary Science Letters* **292,** (2010).
8. Condie, K. C., Aster, R. C. & Van Hunen, J. A great thermal divergence in the mantle beginning 2.5 Ga: Geochemical constraints from greenstone basalts and komatiites. *Geosci. Front.* **7,** 543–553 (2016).
9. Christensen, U. R. & Yuen, D. A. Layered Convection Induced by Phase Transitions. *J. Geophys. Res.* **90,** 10291–10300 (1985).
10. Solheim, L. P. & Peltier, W. R. Mantle phase transitions and layered convection. *Can. J. Earth Sci.* **30,** 881–892 (1993).
11. Li, C., Van Der Hilst, R. D., Engdahl, E. R. & Burdick, S. A new global model for P wave speed variations in Earth's mantle. *Geochemistry, Geophys. Geosystems* **9,** n/a-n/a (2008).
12. Herein, M., Galsa, A. & Lenkey, L. Impact of the Rayleigh number and endothermic phase transition on the time behaviour of mantle avalanches. *J. Geodyn.* **66,** 103–113 (2013).

13. Ringwood, A. E. Phase transformations and mantle dynamics. *Earth Planet. Sci. Lett.* **14,** 233–241 (1972).

14. Hager, B. H. Subducted slabs and the geoid: Constraints on mantle rheology and flow. *J. Geophys. Res. Solid Earth* **89,** 6003–6015 (1984).

15. Tackley, P. J., Stevenson, D. J., Glatzmaier, G. A. & Schubert, G. Effects of multiple phase transitions in a three-dimensional spherical model of convection in Earth's mantle. *J. Geophys. Res.* **99,** 15877 (1994).

16. Zhong, S. & Gurnis, M. Role of plates and temperature-dependent viscosity in phase change dynamics. *J. Geophys. Res.* **99,** 15903 (1994).

17. Karato, S., Riedel, M. R. & Yuen, D. A. Rheological structure and deformation of subducted slabs in the mantle transition zone: implications for mantle circulation and deep earthquakes. *Phys. Earth Planet. Inter.* **127,** 83–108 (2001).

18. King, S. D., Frost, D. J. & Rubie, D. C. Why cold slabs stagnate in the transition zone. *Geology* **43,** 231–234 (2015).

19. Agrusta, R., Goes, S. & van Hunen, J. Subducting-slab transition-zone interaction: Stagnation, penetration and mode switches. *Earth Planet. Sci. Lett.* **464,** 10–23 (2017).

20. Garel, F. *et al.* Interaction of subducted slabs with the mantle transition-zone: A regime diagram from 2-D thermo-mechanical models with a mobile trench and an overriding plate. *Geochemistry, Geophys. Geosystems* **15,** 1739–1765 (2014).

21. Goes, S., Capitanio, F. A. & Morra, G. Evidence of lower-mantle slab penetration phases in plate motions. *Nature* **451,** 981–984 (2008).

22. Stegman, D. R., Farrington, R., Capitanio, F. A. & Schellart, W. P. A regime diagram for subduction styles from 3-D numerical models of free subduction. *Tectonophysics* **483,** 29–45 (2010).

23. Agrusta, R., van Hunen, J. & Goes, S. The effect of metastable pyroxene on the slab dynamics. *Geophys. Res. Lett.* **41,** 8800–8808 (2014).

24. Nakakuki, T. *et al.* Dynamical mechanisms controlling formation and avalanche of a stagnant slab. *Phys. Earth Planet. Inter.* **183,** 309–320 (2010).

25. Tetzlaff, M. & Schmeling, H. The influence of olivine metastability on deep subduction of oceanic lithosphere. *Phys. Earth Planet. Inter.* **120,** 29–38 (2000).

26. Katsura, T. *et al.* Olivine-wadsleyite transition in the system $(Mg,Fe)_2SiO_4$. *J. Geophys. Res. Solid Earth* **109,** (2004).
27. Litasov, K. D. & Ohtani, E. Effect of water on the phase relations in Earth's mantle and deep water cycle. *Geol. Soc. Am. Spec. Pap.* **421,** 115–156 (2007).
28. Litasov, K. D. & Ohtani, E. in *Special Paper 421: Advances in High-Pressure Mineralogy* 115–156 (Geological Society of America, 2007). doi:10.1130/2007.2421(08)
29. Katsura, T. *et al.* Post-spinel transition in Mg2SiO4 determined by high P–T in situ X-ray diffractometry. *Phys. Earth Planet. Inter.* **136,** 11–24 (2003).
30. Holt, A. F. & Becker, T. W. The effect of a power-law mantle viscosity on trench retreat rate. *Geophys. J. Int.* **208,** 491–507 (2017).
31. Arredondo, K. M. & Billen, M. I. Coupled effects of phase transitions and rheology in 2-D dynamical models of subduction. *J. Geophys. Res. Solid Earth* **122,** 5813–5830 (2017).
32. Funiciello, F. *et al. Trench migration, net rotation and slab–mantle coupling. Earth and Planetary Science Letters* **271,** (2008).
33. Capitanio, F., Morra, G. & Goes, S. Dynamic models of downgoing plate-buoyancy driven subduction: Subduction motions and energy dissipation. *Earth Planet. Sci. Lett.* **262,** 284–297 (2007).
34. van Hunen, J. & van den Berg, A. P. Plate tectonics on the early Earth: Limitations imposed by strength and buoyancy of subducted lithosphere. *Lithos* **103,** 217–235 (2008).
35. Korenaga, J. Urey ratio and the structure and evolution of Earth's mantle. *Rev. Geophys.* **46,** RG2007 (2008).
36. van Thienen, P., van den Berg, A. P. & Vlaar, N. J. Production and recycling of oceanic crust in the early Earth. *Tectonophysics* **386,** 41–65 (2004).
37. Sleep, N. H. & Windley, B. F. Archean Plate Tectonics: Constraints and Inferences. *J. Geol.* **90,** 363–379 (1982).
38. Magni, V., van Hunen, J., Funiciello, F. & Faccenna, C. Numerical models of slab migration in continental collision zones. *Solid Earth* **3,** 293–306 (2012).
39. Nisbet, E. G. & Fowler, C. M. R. Model for Archean plate tectonics. *Geology* **11,** 376–379 (1983).
40. Demouchy, S., Tommasi, A., Barou, F., Mainprice, D. & Cordier, P. Deformation of olivine in torsion under hydrous conditions. *Phys. Earth*

Planet. Inter. **202–203,** 56–70 (2012).

41. Fei, H., Wiedenbeck, M., Yamazaki, D. & Katsura, T. Small effect of water on upper-mantle rheology based on silicon self-diffusion coefficients. *Nature* **498,** 213–215 (2013).
42. Hirth, G. & Kohlstedt, D. Rheology of the upper mantle and the mantle wedge: A view from the experimentalists. *Geophys. Monogr.* **138,** 83–105 (2003).
43. Sizova, E., Gerya, T., Brown, M. & Perchuk, L. L. Subduction styles in the Precambrian: Insight from numerical experiments. *Lithos* **116,** 209–229
44. Ranero, C. R., Phipps Morgan, J., McIntosh, K. & Reichert, C. Bending-related faulting and mantle serpentinization at the Middle America trench. *Nature* **425,** 367–373 (2003).
45. Conrad, C. P. & Hager, B. H. Mantle convection with strong subduction zones. *Geophys. J. Int.* **144,** 271–288 (2001).
46. Torii, Y. & Yoshioka, S. Physical conditions producing slab stagnation: Constraints of the Clapeyron slope, mantle viscosity, trench retreat, and dip angles. *Tectonophysics* **445,** 200–209 (2007).
47. Burke, K., Steinberger, B., Torsvik, T. H. & Smethurst, M. A. Plume Generation Zones at the margins of Large Low Shear Velocity Provinces on the core–mantle boundary. *Earth Planet. Sci. Lett.* **265,** 49–60 (2008).
48. Dziewonski, A. M., Lekic, V. & Romanowicz, B. A. Mantle Anchor Structure: An argument for bottom up tectonics. *Earth Planet. Sci. Lett.* **299,** 69–79 (2010).
49. Deschamps, F. & Tackley, P. J. Searching for models of thermo-chemical convection that explain probabilistic tomography. II—Influence of physical and compositional parameters. *Phys. Earth Planet. Inter.* **176,** 1–18 (2009).
50. Tackley, P. J. Dynamics and evolution of the deep mantle resulting from thermal, chemical, phase and melting effects. *Earth-Science Rev.* **110,** 1–25 (2012).
51. Christensen, U. R. & Hofmann, A. W. Segregation of subducted oceanic crust in the convecting mantle. *J. Geophys. Res. Solid Earth* **99,** 19867–19884 (1994).
52. Brandenburg, J. P. & van Keken, P. E. Deep storage of oceanic crust in a vigorously convecting mantle. *J. Geophys. Res.* **112,** B06403 (2007).
53. Faccenda, M. & Dal Zilio, L. The role of solid–solid phase transitions in

mantle convection. *Lithos* **268–271,** 198–224 (2017).

54. McNamara, A. K. & van Keken, P. E. Cooling of the Earth: A parameterized convection study of whole versus layered models. *Geochemistry, Geophys. Geosystems* **1,** n/a-n/a (2000).
55. Davies, G. F. Punctuated tectonic evolution of the earth. *Earth Planet. Sci. Lett.* **136,** 363–379 (1995).
56. Shirey, S. B. & Richardson, S. H. Start of the Wilson Cycle at 3 Ga Shown by Diamonds from Subcontinental Mantle. *Science (80-.).* **333,** 434 LP-436 (2011).
57. Tang, M., Chen, K. & Rudnick, R. L. Archean upper crust transition from mafic to felsic marks the onset of plate tectonics. *Science (80-.).* **351,** 372 LP-375 (2016).
58. Dhuime, B., Hawkesworth, C. J., Cawood, P. A. & Storey, C. D. A Change in the Geodynamics of Continental Growth 3 Billion Years Ago. *Science (80-.).* **335,** 1334 LP-1336 (2012).
59. Gerya, T. Precambrian geodynamics: Concepts and models. *Gondwana Research* **25,** 442–463 (2014).
60. Moresi, L. & Gurnis, M. Constraints on the lateral strength of slabs from three-dimensional dynamic flow models. *Earth Planet. Sci. Lett.* **138,** 15–28 (1996).
61. Zhong, S., Zuber, M. T., Moresi, L. & Gurnis, M. Role of temperature-dependent viscosity and surface plates in spherical shell models of mantle convection. *J. Geophys. Res. Solid Earth* **105,** 11063–11082 (2000).
62. Wang, H., Agrusta, R. & van Hunen, J. Advantages of a conservative velocity interpolation (CVI) scheme for particle-in-cell methods with application in geodynamic modeling. *Geochemistry, Geophys. Geosystems* **16,** 2015–2023 (2015).
63. Turcotte, D. & Schubert, G. *Geodynamics*. (Cambridge University Press, 2002).
64. Xu, W., Lithgow-Bertelloni, C., Stixrude, L. & Ritsema, J. The effect of bulk composition and temperature on mantle seismic structure. *Earth Planet. Sci. Lett.* **275,** 70–79 (2008).
65. Karato, S. & Wu, P. Rheology of the Upper Mantle: A Synthesis. *Science (80-.).* **260,** 771–778 (1993).
66. King, S. D. An evolving view of transition zone and midmantle viscosity.

Geochemistry, Geophys. Geosystems **17,** 1234–1237 (2016).

67. Čížková, H., van den Berg, A. P., Spakman, W. & Matyska, C. The viscosity of Earth's lower mantle inferred from sinking speed of subducted lithosphere. *Phys. Earth Planet. Inter.* **200–201,** 56–62 (2012).

68. Steinberger, B. & Calderwood, A. R. Models of large-scale viscous flow in the Earth's mantle with constraints from mineral physics and surface observations. *Geophys. J. Int.* **167,** 1461–1481 (2006).

69. X., M. J. Haskell [1935] revisited. *J. Geophys. Res. Solid Earth* **101,** 555–569 (1996).

Supplementary material

Table S1 - **List of simulations and results**. The columns show: *Simulation* - the simulation numbers; *Plate age* - the initial subducting plate age in Myr; $(\gamma_{rw\text{-}pv};\ \gamma_{rw\text{-}pv+mw})$ - the Claperon slopes; ΔT_{pot} - the temperature increase, *Ra* - the thermal Rayleigh number (eq. M3), $Rb_{rw\text{-}pv+mw}$ - the endothermic phase Rayleigh number (eq. M5); *P* - the phase buoyancy number (eq. M4); τ_{670} - the time to reach the 670 km; τ_{end} - the time of the end of the simulations; $Slab_{TZ}(\tau_{670})$ - the slab material in the transition zone at the time τ_{670}; D_{TZ} - the slab accumulation rate in the transition zone; $Slab_{LM}$ (τ_{670}) - the slab material in the lower mantle at the time τ_{670}; D_{LM} - the slab accumulation rate in the lower mantle; *Classification* ($D_{TZ/LM}$) - ratio to classify the slab transition zone interaction (eq. 1) and convection style for a pair of young and old plate: 1 = both penetration/ whole mantle convection; 2 = both stagnant/ layered convection, T = old stagnant and young penetrating/ intermitted mantle convection.

Simulations	Plate age Myr	$(\gamma_{rw\text{-}pv};\ \gamma_{rw\text{-}pv+mw})$ Mpa K^{-1}	ΔT_{pot} °C	Ra ($\times10^{10}$)	$Rb_{rw\text{-}pv+mw}$ ($\times10^{10}$)	$P_{rw\text{-}pv+mw}$	t_{670} Myr	τ_{end} Myr	$Slab_{TZ}(\tau_{670})$ km^2	D_{TZ} $km^2\ Myr^{-1}$	$Slab_{LM}(\tau_{670})$ km^2	D_{LM} $km^2\ Myr^{-1}$	Classification $D_{TZ/LM}$	
1	50	(3;-1)	-50	0.09	0.25	-0.04	35.9	121.76	47100	271	2830	2768	0.098	1
2	100			0.09	0.25	-0.04	21.08	106.67	48000	405	1440	4124	0.098	
3	50	(4;-2)		0.09	0.25	-0.07	43.42	115.83	45700	956	1770	1536	0.623	T
4	100			0.09	0.25	-0.07	17.64	139.68	37000	1940	1330	1867	1.040	
5	50	(5;-3)		0.09	0.25	-0.11	43.47	112.64	43700	1452	2400	996	1.457	2
6	100			0.09	0.25	-0.11	17.25	118.03	35400	2535	1770	1153	2.197	
7	50	(3;-1)	0	0.20	0.53	-0.04	13.17	81.33	30600	297	2050	3202	0.093	1
8	100			0.20	0.53	-0.04	10.59	64.45	39900	511	2470	5498	0.093	
9	50	(3.5;-1.5)		0.20	0.53	-0.05	13.06	84.32	30900	306	1680	3199	0.096	1
10	100			0.20	0.53	-0.05	10.16	67	40400	781	2100	5164	0.151	
11	50	(4;-2)		0.20	0.53	-0.07	12.74	83.07	31000	436	1590	3272	0.133	T
12	100			0.20	0.53	-0.07	10.01	112.56	41000	2976	2090	2327	1.279	
13	50	(4.5;-2.5)		0.20	0.53	-0.09	12.59	86.43	31400	572	1580	3122	0.183	T
14	100			0.20	0.53	-0.09	9.96	80.21	41100	2638	1870	1766	1.493	
15	50	(5;-3)		0.20	0.53	-0.11	12.52	92.24	31300	1127	1500	1956	0.576	T
16	100			0.20	0.53	-0.11	9.6	84.4	41300	2993	1890	1067	2.805	
17	50	(4;-2)	50	0.41	1.08	-0.07	7.07	86.63	27700	-4	0	4754	-0.001	1
18	100			0.41	1.08	-0.07	5.71	68.53	36900	1290	969	6584	0.196	
19	50	(5;-3)		0.41	1.08	-0.11	6.5	111.77	27300	457	0	3022	0.151	1
20	100			0.41	1.08	-0.11	5.27	89.7	36800	570	443	6489	0.088	
20a (μ_{cut} 10^{23})	100			0.41	1.08	-0.04	5.22	85.38	36900	302	369	6955	0.043	N/A
20b (μ_{cut} 5×10^{22})	100			0.41	1.08	-0.04	5.19	85.2	37200	1781	221	4812	0.370	
20c (μ_{cut} 10^{22})	100			0.41	1.08	-0.07	4.96	70.69	37700	4817	0	2115	2.277	
21	50	(3;-1)	100	0.83	2.11	-0.07	5.55	25.61	28200	-91	1120	7397	-0.012	1
22	100			0.83	2.11	-0.11	3.73	24.83	33000	93	618	9938	0.009	
23	50	(4;-2)		0.83	2.11	-0.11	5.1	35.86	29200	-296	166	8234	-0.036	1
24	100			0.83	2.11	-0.04	3.47	38.84	33800	381	0	10970	0.035	
25	50	(5;-3)		0.83	2.11	-0.04	4.62	68.46	29100	-124	0	5263	-0.024	1
26	100			0.83	2.11	-0.07	3.12	23.47	33500	2336	0	8664	0.270	
27	50	(3;-1)	200	3.02	7.11	-0.07	2.82	11.84	20600	-173	304	11258	-0.015	1
28	100			3.02	7.11	-0.11	2.17	12.62	32900	-553	526	13280	-0.042	
29	50	(4;-2)		3.02	7.11	-0.11	2.65	13.92	20600	-164	185	13280	-0.012	1
30	100			3.02	7.11	-0.11	2.02	20.17	33200	411	28	13673	0.030	
31	50	(5;-3)		3.02	7.11	-0.11	2.41	28.37	19600	1788	37	5181	0.345	1
32	100			3.02	7.11	-0.11	1.77	21.5	32300	191	0	17539	0.011	

Figure S1 – **Slab dynamics classification at different mantle temperatures**. (a) Slab accumulation rates in the transition zone (D_{TZ}) and in the lower mantle (D_{LM}) for all simulations. The open/solid symbols represent the models with the initial subducting plates of 50/100 Myr old, respectively. The symbol size and the colour represent the Clapeyron slopes, and mantle temperature respectively (see Figure 4). The asterisk, the cross and the plus symbols represents the additional cases with a cut off viscosity below 400 km reduced to 10^{23} Pa▪s, 5×10^{22} Pa▪s, and 10^{22} Pa▪s, respectively. (b,d) Accumulation

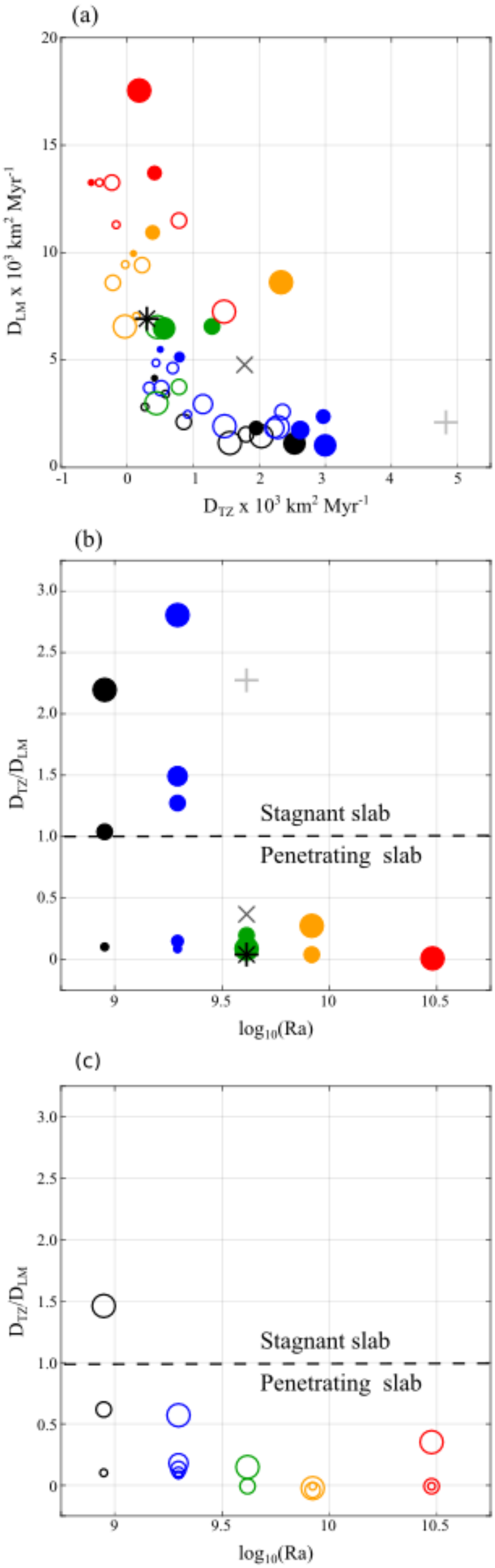
(a)
D_{LM} x 10^3 km^2 Myr^{-1}
D_{TZ} x 10^3 km^2 Myr^{-1}
(b)
D_{TZ}/D_{LM}
Stagnant slab
Penetrating slab
$\log_{10}$(Ra)
(c)
D_{TZ}/D_{LM}
Stagnant slab
Penetrating slab
$\log_{10}$(Ra)

Model including non-Newtonian rheology and 60 wt% olivine

The rheological model is assumed to be a combination of diffusion (μ_{diff}), dislocation (μ_{disl}) creep, and a pseudo-brittle yield stress rheology (μ_y). The effective viscosity μ_{eff} is than calculated from the viscosities of the individual mechanisms as:

$$\mu_{eff} = \min\left(\mu_{diff}, \mu_{disl}, \mu_y\right) \tag{S1.a}$$

with

$$\mu_{disl} = A_{disl}^{\frac{1}{n}} \exp\left(\frac{E_{disl} + PV_{disl}}{nRT}\right) \dot{\varepsilon}_{II}^{\frac{1-n}{n}} \tag{SI.b}$$

To facilitate comparison between the models, we choose the rheological parameters to yield a similar average upper and lower mantle viscosity as when only Newtonian rheology is assumed. The rheological parameter values are listed in Table S2. The density contrast ($\Delta\rho$) for the olivine solid-solid phase transitions are reduced to 60% of those in Table M1 to 150 kg m^{-3} for the ol-wd and of 210 kg m^{-3} for the rg-pv+mw.

Table S2 – **List of rheological parameters**

Symbol	Meaning	Unit	Value
	Diffusion creep		
A_{diff}	Pre-exponential upper mantle	Pa·s	6.47×10^{9}
	Pre-exponential lower mantle		1.87×10^{14}
E_{diff}	Activation energy upper mantle	J·mol^{-1}	3×10^{5}
	Activation energy lower mantle		2×10^{5}
V_{diff}	Activation volume upper mantle	m^{3}·mol^{-1}	4×10^{-6}
	Activation volume lower mantle		1.5×10^{-6}
$\Delta\mu_{lower/upper}$	Viscosity jump	-	10
	Dislocation creep		
A_{disl}	Pre-exponential upper mantle	Pa^{n}·s	5×10^{16}
E_{dsl}	Activation energy upper mantle	J·mol^{-1}	5×10^{5}
V_{disl}	Activation volume upper mantle	m^{3}·mol^{-1}	11×10^{-6}
n	Exponetial factor		3.5

Figure S2 – **Slab transition zone interaction in a mantle deforming with dislocation creep.** (a,b) Bi-modal slab-transition zone interaction at present-day temperature conditions for an endothermic phase transition of -2 MPa·K^{-1} is illustrated by two snap shots each of the viscosity structure for the subduction of young (a) and old (b) plates. (c,d) Illustrate how in a model with the same parameters slab behaviour changes at higher mantle temperature (ΔT_{pot} = 50 °C) (c, young and d, old plate) . In these cases both plates sink readily into the lower mantle. These results agree with the model when only a Newtonian rheology is considered.

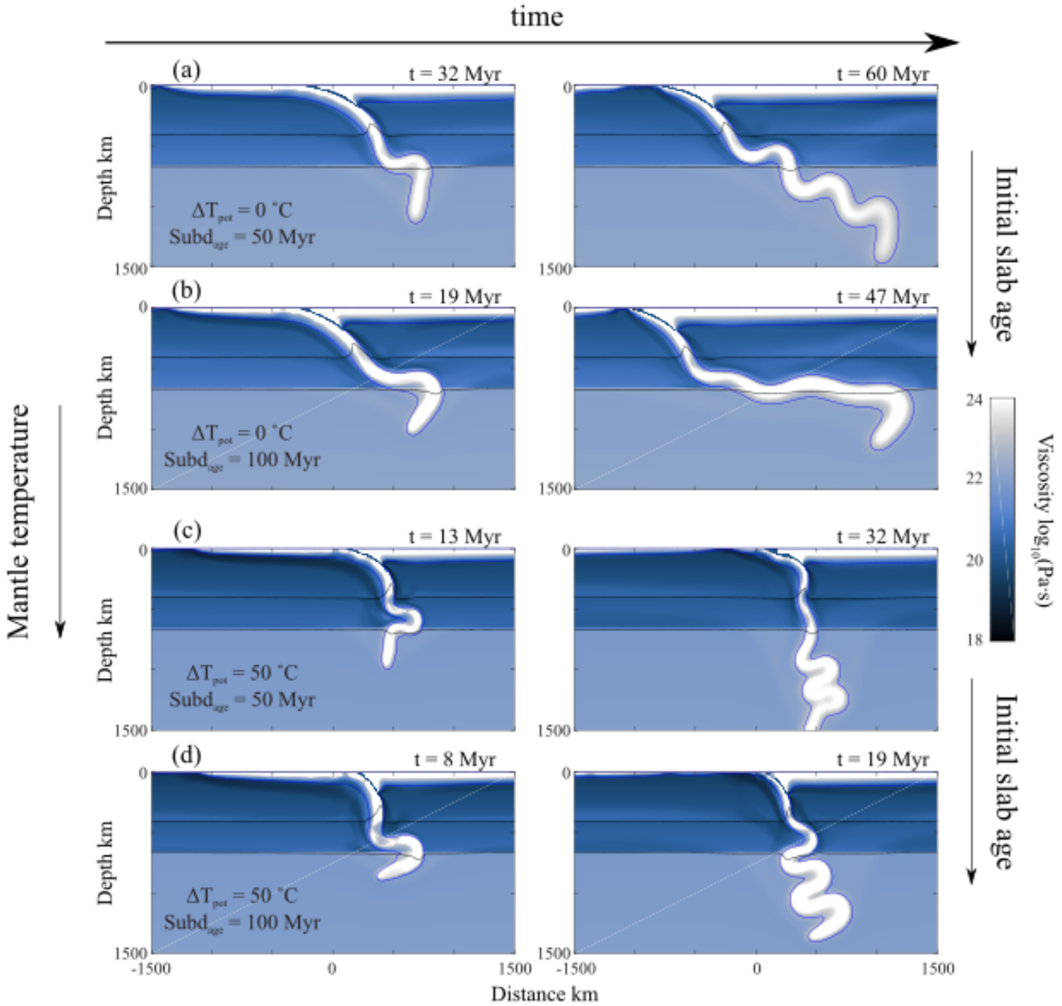

Figure S3 – **Dominant deformation mechanism during slab sinking for non-Newtonian models.** Same snapshots as Figure S2 but illustrating the dominant (weaker) deformation mechanism. Dislocation creep is limited to the asthenosphere and around the slab where stresses are highest.